Journal of Applied Polymer Science

WILEY

Applied Polymer Science

RESEARCH ARTICLE OPEN ACCESS

Photopolymerization-Induced Phase Separation in (Meth)Acrylate-Based Photopolymers From a Characterization Point of View

Mojtaba Ahmadi[1] | Katharina Ehrmann[2] | Michael Göschl[2] | Philipp Schlossgangl[1] | Thomas Koch[1] | Robert Liska[2] | Jürgen Stampfl[1]

[1]Institute of Materials Science and Technology, TU Wien, Vienna, Austria | [2]Institute of Applied Synthetic Chemistry, TU Wien, Vienna, Austria

Correspondence: Mojtaba Ahmadi (mojtaba.ahmadi@tuwien.ac.at)

Received: 21 January 2025 | **Revised:** 22 April 2025 | **Accepted:** 19 May 2025

Funding: The authors received no specific funding for this work.

Keywords: microscopy | photochemistry | structure–property relationships

ABSTRACT

This work investigates the development of photopolymerization-induced phase separation (PhIPS) in methacrylate-based photopolymers. Bisphenol A ethoxylated dimethacrylate (BisEMA) was copolymerized with urethane-based diacrylate diluted in isobornyl acrylate (UI) under UV irradiation, using diphenyl-(2,4,6-trimethylbenzoyl) phosphine oxide (TPO) as a photoinitiator. Optical changes in the cured copolymers were monitored in real time with a custom setup. NIR-photorheometry, photo-differential scanning calorimetry, dynamic mechanical analysis, scanning electron microscopy, and atomic force microscopy in both topography and phase imaging modes were employed to characterize the PhIPS effect on network development and microstructure. The correlation between the microstructure of copolymers with varying BisEMA/UI ratios and their bulk properties was studied through tensile and dynstat impact tests. Results showed that up to 20% UI enhances the elongation at break of BisEMA without compromising strength. At higher monomer/oligomer ratios, phase separation led to a strength–ductility trade-off. The study also addresses the influence of AFM sample preparation on correlating phase imaging results to the local stiffness distribution.

1 | Introduction

Material processing through lithography-based additive manufacturing (AM) relies on photopolymerization reactions to transform liquid formulations into precisely defined three dimensional structures [1–3]. The majority of these formulations utilize (meth)acrylate-based monomers due to their high reactivity and rapid ambient curing, proper mechanical properties, and biocompatibility [4–6]. The structural diversity of available (meth)acrylate-based monomers and oligomers, combined with the high precision offered by stereolithographic techniques, makes these systems attractive for a variety of applications [7].

Multifunctional (meth)acrylate-based monomers actively participate in light-initiated chain growth polymerization and form crosslinked polymer networks. Other monomers, including reactive diluents and oligomers, are commonly incorporated for adjusting mechanical behavior and facilitating processing [6]. The microstructure of the resulting polymer, which dictates its performance, is modulated by the interactions among these components [8]. Such interactions may also lead to photopolymerization-induced phase separation (PhIPS), wherein marginal incompatibility of reacting species leads to the formation of distinct domains with contrasting mechanical and optical properties [9]. The morphology and mechanical contrast of resulting domains significantly affect the overall performance and appearance of the polymer, making PhIPS a critical chemical tool in photopolymer-related technologies [10–14]. PhIPS has thereby been employed in the formation of polymer-dispersed liquid crystals [15, 16], electrically conducting photopolymers [10], perforating films [17], 3D printed multicomponent glasses [18], biomimicking [19], shape memory [20], and controlling the nanostructure of 3D printed polymers [21].

More importantly, by introducing heterogeneity, PhIPS can enhance the fracture toughness and ductility of photopolymers [22, 23]. This strategy reflects the toughening mechanisms observed in heterogeneous engineering thermoplastics (e.g., ABS and SBS), composites, and high-strength biomaterials (nacre, bone, teeth, etc.) wherein the appropriate combination of soft and hard phases allows for a compromise between the challenged strength and ductility [24–26].

A clear understanding of how PhIPS can tune the mechanical performance of photopolymers relies on its thorough characterization. This study therefore investigates the evolution of PhIPS in a phase-separable system and correlates the resulting microstructures with changes in thermomechanical and fracture behavior.

Phase-separated morphologies are influenced by several formulation and processing parameters. Among these, the monomer composition ratio plays a critical role, as variations in functionality and molecular weight affect both the chemical incompatibility and polymerization kinetics [27]. A high crosslinking rate accelerates gelation, which can arrest the development of PhIPS to a large extent. Therefore, strategies that delay gelation, such as adjusting the photoinitiator concentration, irradiation intensity, curing temperature, and incorporating chain transfer agents are commonly used to promote or control phase separation [13, 28–32]. Thorough characterization of PhIPS is hence essential not only for controlling the morphology but also for elucidating the structure–property relationships [33–35].

In this work, we designed a methacrylate-based system conceptually inspired by the multiphase structure of acrylonitrile butadiene styrene (ABS), a material widely known for its balance of stiffness, strength, and ductility, but not typically achievable in photopolymer networks [36]. Bisphenol A ethoxylated dimethacrylate (BisEMA) monomers, commonly used in restorative dental composites, were chosen to represent the rigid phase, while an aliphatic urethane diacrylate oligomer (UDA) diluted in isobornyl acrylate (IBOA)—hereafter referred to as UI—was selected for its flexible, rubbery-like character. The entire system's polymerization was triggered by the photoinitiator diphenyl-(2,4,6-trimethylbenzoyl) phosphine oxide (TPO). The evolution of PhIPS within the polymerizing system was characterized using real-time turbidity measurements and atomic force microscopy (AFM), with the latter providing unique insights into the contrast in rigidity between phases. Photo-differential scanning calorimetry (photo-DSC) and dynamic mechanical analysis (DMA) were employed to investigate the thermomechanical properties, while tensile and impact tests provided further understanding of the corresponding mechanical performance of resulting photopolymer specimens.

2 | Experimental Section

2.1 | Materials

Table 1 shows the composition of formulations used in this study. The chemical structure of each component is shown in Figure 1.

2.2 | Methods

To formulate the photopolymers, a high-speed mixer was employed to stir the formulations vigorously at a rotational speed of 3500 rpm for 10 min. To eliminate entrapped air from the formulations, each formulation was subjected to a degassing procedure in a vacuum chamber for approximately 10 min. Degassed formulations were then transferred into transparent sample

TABLE 1 | Formulation and chemical structure of the used materials. BISEMA was formulated with varying amounts of a commercially available mixture of UDA/IBOA at a fixed ratio of 40/60 (w/w), used as received.

Component	Chemical structure	Amount [wt.%]	Molecular weight [g/mol]	Refractive index at 25°C	Supplier	Batch no.	Function
BisEMA	Bisphenol A ethoxylate dimethacrylate	50–100	496	1.5364	Sartomer	SR348C	Crosslinker (difunctional monomer)
UDA	Urethane diacrylate	0–50	30,000	1.477	Miwon	UA5216	Toughener (difunctional monomer)
IBOA	Isobornyl acrylate		208.3				Reactive diluent (monofunctional monomer)
TPO	Diphenyl (2,4,6-trimethylbenzoyl) phosphine oxide	1	—	—	Lambson (Sartomer)	20,190,151	Norrish Type I photoinitiator

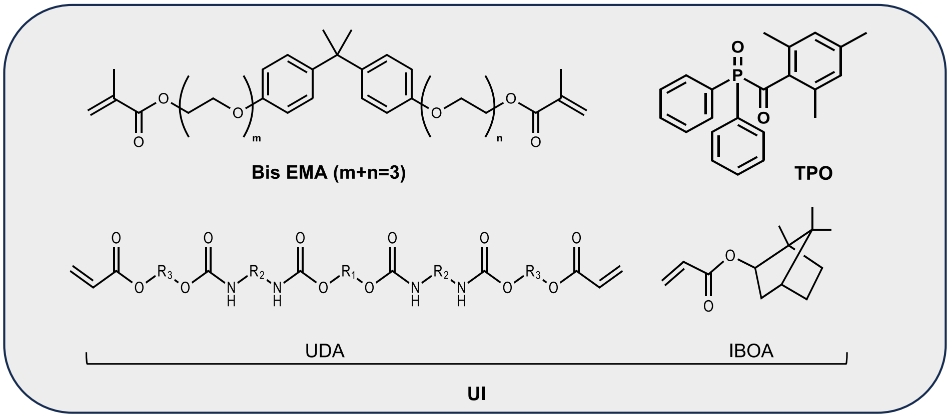

FIGURE 1 | Chemical structure of BisEMA, UDA, IBOA, and TPO. For the urethane diacrylate (UDA), the R groups typically represent a flexible polyether or polyester diol residue (R_1), aliphatic diisocyanate residue contributing to UV stability (R_2), and a hydroxyalkyl acrylate spacer (R_3). The exact chemical composition is not disclosed by the supplier. [Color figure can be viewed at wileyonlinelibrary.com]

vials and left undisturbed in a UV-isolated environment overnight to ensure proper uniformity before curing. Following the resting period, the formulations were transferred into a transparent silicone mold, meticulously designed to shape resins according to the geometries dictated by the corresponding standards for mechanical tests, including tensile, impact, and DMA tests. To counteract the negative effects of oxygen inhibition on polymerization efficiency, the formulations were covered with non-adhesive transparent fluorinated ethylene propylene films, which effectively shield the formulation from contact with atmospheric oxygen during the photopolymerization process.

The curing process was conducted in a UV chamber (UViTRON Intelliray 600), equipped with a metal halide-type lamp designed to emit light within the wavelength range of 320–390 nm. All formulations were cured at an intensity of 57 mW cm^{-2} for 120 s. Thereafter, specimens were submerged in isopropanol and sonicated for 10 min to ensure complete removal of any sticky residues from their surfaces.

2.2.1 | Real-Time Transparency Monitoring

To accurately monitor and quantify the transparency of formulations during the photopolymerization, a customized transparency monitoring setup was developed (Figure 2a,b).

A few milliliters of the formulation were deposited between two glass slides separated by a 200-μm spacer and positioned perpendicular to the path of the red light. The red light continually traveled toward the detector without interacting with the material. To establish a reference point, the initial receiving intensity (in voltage) of the red light was denifed as representing 100% transparency. Real-time transparency monitoring was then conducted via red light intensity tracking upon activation of the UV light source (wavelength range: 320–390 nm, applied intensity; 28 mW cm^{-2}), which is delivered to the formulation via reflection by the dichroic mirror to initiate the polymerization. The evolving change in transparency driven by phase separation was recorded in real time via the Arduino program as the intensity of the red light reaching the detector underwent continuous changes. The resulting transparency–time curves provide diagnostic data including the phase separation onset, its duration, and ultimate transparency (Figure 2c). The phase separation onset was thereby operationally defined as the point at which transparency decreased to 98% from the initial transparency plateau [22]. Moreover, the PhIPS duration was calculated by determining the time point at which the transparency began to remain constant. The corresponding transparency value was taken as a measure of the ultimate transparency.

2.2.2 | Photorheology

Photorheology complements a standard rheology setup with the possibility to irradiate the measured formulation through the transparent bottom plate to observe rheological changes of storage and loss modulus during curing. Simultaneously, the conversion is measured by infrared (IR) spectroscopy. A detailed description of the setup is given in [37].

For the presented measurements, a parallel plate rheology stamp with a diameter of 25 mm was used with a gap size of 0.2 mm. Approximately 140 μL of the formulations were transferred onto the UV-transparent bottom plate of the rheometer using an Eppendorf pipette. The plate had been previously covered with polyethylene tape. The samples were irradiated with a filtered Hg lamp (Omnicure) with a wavelength range of 320–500 nm. The irradiation time was set to 300 s with a light intensity of 28 mW cm^{-2}. NIR data were evaluated by performing a baseline correction on the data set (concave rubber band method, 10 iterations), followed by integrating the curve from 6228 to 6100 cm^{-1}.

2.2.3 | Photo-Differential Scanning Calorimetry (Photo-DSC)

Photo-DSC monitors evolving heat during the photopolymerization as a measure for reactivity [38]. For this purpose, the formulation in the DSC crucible is irradiated twice through a transparent coverslip. While the first irradiation period indicates the sum of heat flows of the photopolymerization reaction and the heat evolving through irradiation, the second irradiation period is conducted when the photopolymerization reaction

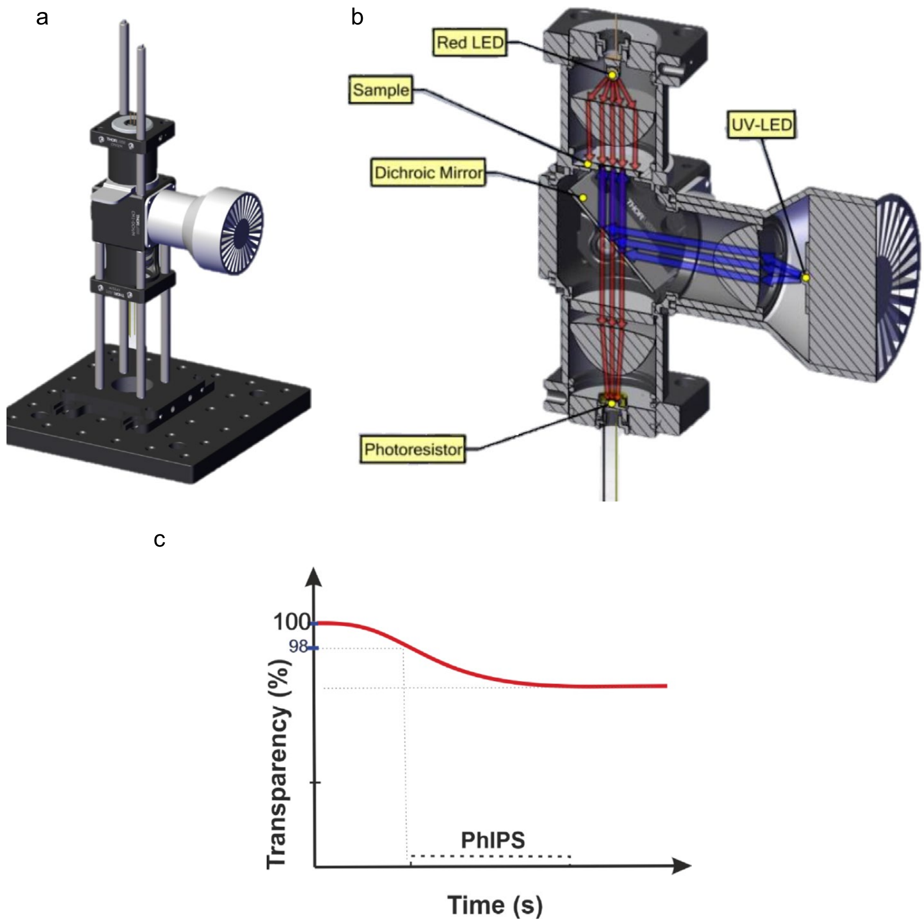

FIGURE 2 | Closed system designed for monitoring the PhIPS in initially transparent formulations: (a) an overview of the setup, (b) cross section of the system, and (c) a schematic of the transparency changes over time. [Color figure can be viewed at wileyonlinelibrary.com]

has subsided and hence only indicates the heat flow resulting from the irradiation heat. By deducting the second measurement from the first, the pure heat of photopolymerization is obtained as the peak area (ΔH_p). Additionally, the time until the maximum heat evolution is reached (t_{max}) and the time until 95% conversion is reached (t_{95}) can be determined as measures for reactivity (Figure 3).

From the theoretical heat of polymerization ($\Delta H_{0,P}$), which is 56 kJ mol^{-1} for methacrylates [39] and 80.5 kJ mol^{-1} for acrylates [40], the double bond conversion (%) can be deduced using Equation (1):

$$DBC = \frac{\Delta H_P}{\Delta H_{0,P}} \tag{1}$$

For the presented measurements, 10–15 mg of the formulation was accurately weighed into an aluminum DSC crucible and covered with a glass coverslip. A light source with a wavelength range of 320–500 nm and an intensity of 27–28 mW cm^{-2} was used to irradiate the sample. Irradiation started after 60 s and the sample was irradiated for 300 s. A second analogous irradiation period was performed, and the measurements were subtracted from each other to achieve the previously described baseline correction.

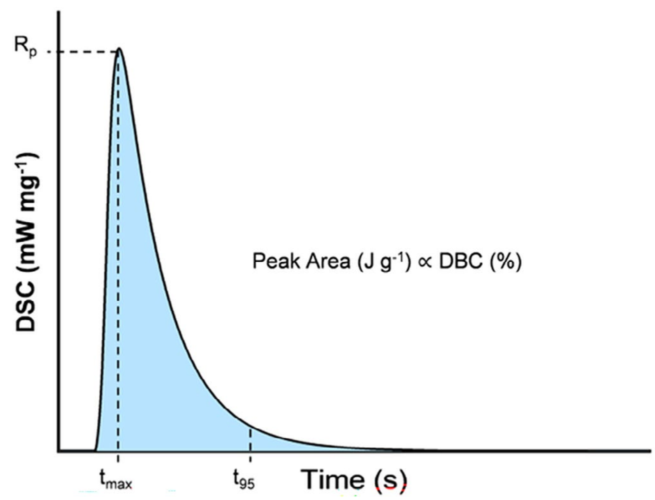

FIGURE 3 | The variation of DSC signal (mW mg^{-1}) over time (seconds). Key parameters such as height (h), onset time (t_{max}), and end time can be identified from the curve. [Color figure can be viewed at wileyonlinelibrary.com]

2.2.4 | Dynamic Mechanical Analysis

DMA was employed to study structural heterogeneities via the thermomechanical behavior of resulting bulk polymer specimens. The measurements were conducted using the DMA device Q800 (TA Instruments, DE, USA), and the accompanying testing software Trios, (TA Instruments, DE, USA).

For the 3-point bending mode DMA, rectangular prism samples in the size of $20\times2\times2\,mm^3$ were subjected to a constant frequency of 1 Hz and an amplitude of 20 μm for all samples, which were preloaded with a force of 0.1 N during temperature variation ranging from −50°C to 200°C. The samples were initially cooled to −50°C using liquid nitrogen and maintained at this temperature for 5 min to ensure a uniform temperature distribution. Subsequently, the samples were heated to 200°C at a controlled heating rate of 3°C min^{-1}. The value of tan δ and its corresponding temperature were taken as representatives of damping behavior and T_g, respectively. Moreover, the network irregularity of different BisEMA/UDA compositions was studied. This value was obtained from the full width at half maximum (FWHM) of the tan δ peak.

2.2.5 | Scanning Electron Microscopy

The representation of fracture surfaces, down to the nanometer range, is achieved using a scanning electron microscope (SEM) (Zeiss EVO 10) equipped with a tungsten hairpin cathode for electron emission. Samples were coated with gold by sputtering for 1 min at a distance of 4 cm from the cathode in a vacuum. Electron emission was achieved from the cathode at acceleration voltages of up to 30 kV, and was subsequently focused onto a specific point on the sample via magnetic lenses. Different electron-surface interactions result in surface imaging by means of detected secondary electrons and backscattered electrons, among others. For optimal imaging, a working distance of 8.5 mm from the electron beam exit to the sample surface should be maintained. Deviations above or below this distance make it extremely difficult to achieve focused images.

2.2.6 | Atomic Force Microscopy

Microstructure characterization was performed using AFM in tapping mode through a Park Systems XE7 (Korea). Topography and phase imaging channels were recorded, and the resulting data were then analyzed using the built-in XEI data processing tool.

Before imaging, a portion of the fractured tensile test specimens was sonicated in isopropanol to remove any sticky residues that could interfere with the cantilever's tapping motion. The samples were then immobilized on a metallic base using sand paste.

The fracture surfaces were scanned over an area of $20\times20\,\mu m^2$. For phase imaging, smoother areas within these images, sized $2\times2\,\mu m^2$, were selected and scanned. The resolution of the scanned area was 256 × 256 pixels, with a scan rate of 0.7 Hz. The cantilever used (AC160TS Olympus) featured a tetrahedral silicon tip with an approximate tip radius of 7 nm, a spring constant of 26 $N\,m^{-1}$, and a free resonance frequency close to 300 kHz.

2.2.6.1 | Surface Preparation Techniques. To evaluate the effect of sample preparation on the quality of phase imaging, the fracture surfaces were further subjected to polishing and ultramicrotomy.

2.2.6.1.1 | Polishing and Grinding. The fracture surfaces were further subjected to polishing and ultramicrotomy to evaluate the effect of sample preparation on the quality of phase imaging. Polishing was performed using a Tegramin-30 polishing machine from Struers (Denmark) with a downward force of 10 N at 150 rpm. Initially, the fracture surfaces were sanded down to an even surface using a rough plate in the presence of water. This was followed by polishing with a 3 μm diamond paste and DP-lubricant blue (Struers) for 10 min. After polishing, the samples were sonicated in isopropanol for 5 min.

2.2.6.1.2 | Cryo-ultramicrotomy. Smooth cross sections of the samples were also prepared using cryo-ultramicrotomy with the mentioned parameters in Table 2. An initial trimming step was performed using a Diatome CT 620 trimming knife to reduce the sample size, bringing the width to less than 1 mm and the length to less than 2 mm. This was necessary because the cut surface of the samples was too large for uniform sectioning. This preliminary trimming offers the advantage of minimizing excessive cutting forces, thereby enhancing the cutting quality. Subsequently, the surface of the pre-trimmed samples was removed via cryo-ultramicrotomy employing the Diatome MA 1063 diamond knife. Optimal cutting parameters were determined for the specific material characteristics, resulting in the cutting of brittle samples at lower temperatures and ductile samples at relatively higher sub-zero temperatures. The maximum allowable cutting speed is constrained to 1 $mm\,s^{-1}$ by the knife manufacturer and further limited by the RMC ultramicrotome PowerTome PT-PC to 0.1 $mm\,s^{-1}$. Additionally, the manufacturer specifies a knife angle of 6°. Adjustable parameters for microtomy were confined to four main variables: knife temperature, sample temperature, cutting speed in

TABLE 2 | Applied ultramicrotome parameters to the individual BisEMA/UI photopolymer's composition at knife angle 6°.

BisEMA/UI ratio	Knife temperature (°C)	Sample temperature (°C)	Cutting thickness (nm)	Feed speed ($mm\,s^{-1}$)
100:00	−20	−20	60	0.2
90:10	−80	−80	350	0.8
80:20	−80	−80	300	0.8
70:30	−100	−100	450	0.6
50:50	−100	−100	250	0.6

the range of 0.1–1 mm s^{-1}, and feed thickness. After sectioning the samples using the cryo-ultramicrotome, they were subjected to ultrasonic cleaning in a bath containing ethanol for 5 min at a frequency of 35 kHz. This procedure was aimed at eliminating contaminants and unreacted monomers, which can interrupt the course of AFM imaging.

2.2.6.2 | Data Analysis. From topography imaging, average roughness (R_a) and peak-to-valley roughness (R_{pv}) were calculated by the built-in software. Moreover, horizontal profile line analysis was performed to provide initial insights into the extent of irregularities on the fracture surface. Phase imaging visualized the relative cantilever damping after tapping the surface. The resulting image and the generated histogram were used to study phase contrasts, specifically the phase lag of the cantilever's oscillation relative to the initial signal applied to the cantilever's piezo driver.

2.2.7 | Tensile Test

Tensile tests were conducted on three specimens of each formulation to evaluate the response of the photopolymer to gradually applied stress. The tests were performed using a Zwick Z050 tensile testing machine (Germany), following the guidelines outlined in ISO 527-1. The specimens were prepared in 5B geometry and subjected to a constant stretching rate of 1 mm min^{-1} to ensure gradual and controlled deformation. Young's modulus, tensile strength, and elongation at break were obtained from the results of these measurements.

2.2.8 | Dynstat Impact Test

Eight unnotched Dynstat specimens typically sized 15 × 10 × 4 mm (thickness × width × height) were prepared for testing. These specimens were fixed vertically between two thrust blocks and subjected to an impact of a 1 J hammer. The impact strength (a_{dU}) was calculated by measuring the height reached by the pendulum after releasing it from the starting point and successfully breaking the specimen by using this formula:

$$a_{dU} = \frac{E_c}{d \times b} . 10^3 \tag{2}$$

where the impact strength a_{dU} (kJ m^{-2}) becomes related to the absorbed energy E_c (J) to fracture the specimen. d and b represent the thickness and width of the specimen in mm, respectively.

3 | Results and Discussion

Proper characterization of PhIPS in multicomponent methacrylate systems requires a profound understanding of their network development. Photopolymerization of multifunctional methacrylate monomers initiates through crosslinking upon cleavage of photoinitiator molecules sensitive to specific wavelengths of light. The resulting crosslinked networks exhibit varying degrees of crosslinking density due to the rapid reaction rates, irregular spatial chain propagation, and physical intersegment interactions [41]. Within these networks, segments of polymer chains that fold back on themselves and form loops, the interpenetration of polymer chains that make entanglements, and pendant groups attached to the polymer backbone all contribute to a broad distribution of crosslinked domain sizes [5]. In multicomponent methacrylate systems, network development is more complex due to the simultaneous polymerization of monomers with different reactivities and compatibilities [42]. While thermodynamics may favor the formation of separated phases in such systems, early gelation—resulting from rapid and extensive crosslinking—minimizes diffusion and stabilizes the developing network despite potential thermodynamic instability [43]. Early gelation also plays a crucial role in the evolution of shrinkage stresses, which are caused by the volume decrease essentially due to the transformation of Van der Waals distances between monomers in the uncured state to covalent bond distances in the cured solid state [22, 37, 44]. Adopting systems highly susceptible to phase separation as well as delaying the gel point are among the factors that contribute to higher PhIPS levels [31, 45–47].

The phase-separated photopolymer may accordingly appear translucent or opaque when the formed domains are big enough to refract visible light [48]. Phase-separated photopolymers may exhibit varying levels of translucency or opacity depending on the size of the domains that refract visible light. Accurate characterization of PhIPS in methacrylate systems, however, necessitates using additional techniques such as AFM and DMA, which are discussed in the following.

3.1 | Development of Phase Separation in BisEMA-UI Formulations

The prepared formulations in BisEMA/UI systems initially appeared clear and homogeneous when stored in glass vials for 48 h. However, noticeable optical changes were observed in their copolymerized forms (Figure 4 left). The onset and degree of transparency loss were measured systematically across varying BisEMA/UI composition ratios (Figure 4 right). Pure BisEMA exhibited a slight decrease in transparency compared to its initial liquid state, likely due to the formation of microgels with refractive indices differing from the uncured resin [9]. Increased opacity was evident in formulations with higher UI content in the BisEMA/UI copolymers. Specifically, formulations with a 50:50 ratio of BisEMA to UI showed a 25% drop in transparency, indicating pronounced phase separation (PhIPS). UI comprises 60% monofunctional IBOA as a reactive diluent. Despite the initial compatibility, UI components may experience reduced compatibility as they participate in crosslinking reactions with BisEMA, leading to altered supramolecular interactions.

3.2 | Polymerization Kinetics and Transparency Monitoring

The final morphology of the polymerized systems is governed by the interplay between gelation (a kinetic process) and photopolymerization-induced phase separation (PhIPS), a thermodynamic process [22, 49]. Early gelation physically stabilizes the system before the phase separation dynamics lead to

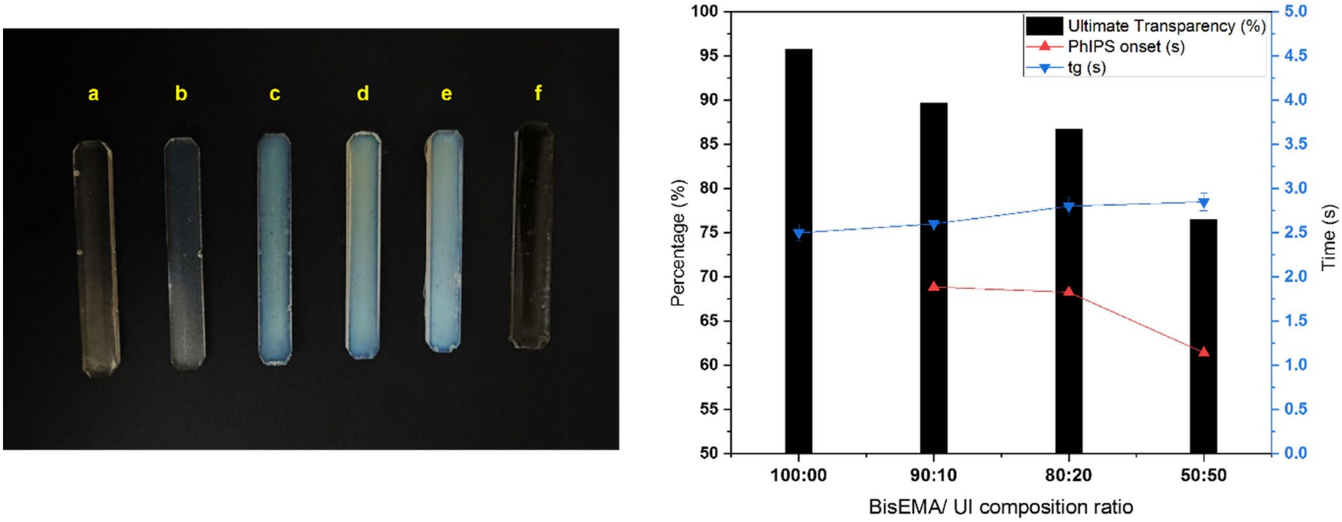

FIGURE 4 | (Left) Visual appearance of photopolymers with varying BisEMA to UI ratios: (a) 100:00, (b) 90:10, (c) 80:20, (d) 70:30, (e): 50:50, and (f) 00:100. (Right) Ultimate transparency and PhIPS onset for photopolymers with different BisEMA/UI composition ratios. [Color figure can be viewed at wileyonlinelibrary.com]

the formation of fully distinct phases. This suppressive effect contradicts the PhIPS tendency, as it limits the mobility of the system and reduces the extent to which components can move and separate further [50]. To evaluate the reactivities of such multicomponent systems, NIR photorheology was employed to measure gelation times. The time until gelation, also referred to as gel point (t_g) was determined by tracking the development of storage and loss modulus curves during light exposure, identifying the crossover of these curves throughout the curing reaction. Results are shown in Figure S1.

The expected high reactivity of the formulation, however, led to challenges in identifying precise differences due to insufficient resolution in the region of interest (Figure S2). Figure 3 (right) illustrates the observed gelation times, revealing slight differences in gel points for all BisEMA/UI formulations, with values ranging between 2.5 and 2.8 s.

Notably, upon photopolymerization, pure BisEMA exhibits more rapid crosslinking than its copolymers with UI, resulting in faster gelation (2.5–2.6 s). As the difunctional methacrylate BisEMA is replaced by increasing amounts of less reactive UI, a slight upward trend in tg (up to 2.8 s) is observed. UI contains the high molecular weight component UDA and a high weight fraction of the monofunctional reactive diluent IBOA, which both favor slower crosslinking. However, both monomers contain the more reactive acrylate group, which, in addition to the higher viscosity of UI compared to BisEMA (20 Pa·s at 25°C vs. 810 mPas) can contribute to faster gelation. Among these competing factors, the monofunctionality of IBOA most likely has the greatest influence, as it leads to a slower immobilization of the network during polymerization. This effect shifts t_g to higher values with increasing weight fractions of UI [12, 51].

To elucidate the interplay between gelation and PhIPS, the transparency of the resins during photopolymerization was monitored. While the rapid nature of the crosslinking reaction in multifunctional (meth)acrylates limits both the precise determination of t_g and the PhIPS onset, the developed setup provides sufficiently accurate and consistent data to capture the initial stages of phase separation. As shown in Figure 4 (right), the use of a contractual threshold suggests that PhIPS starts within the first 2 s prior to gelation in all BisEMA/UI systems, and even earlier in those containing higher UI fractions. This suggests that delayed gelation is not the only factor extending the duration of PhIPS; rather, such formulations are also more prone to initiate phase separation earlier. Representative transparency-time curves are provided in Figure S3. Moreover, the partial recovery of transparency, which sometimes occurs after the formulation loses substantial transparency due to partial post-matching of phases, was not detected in the measured formulations during the short curing duration (6–7 s) [9, 22].

Nonetheless, comparing the transparency-time curves with t_g (Figure 4 right) reveals that the transparency loss due to PhIPS onset consistently precedes gelation onset for all BisEMA/UI systems.

Additionally, the abundance of reactive sites in pure BisEMA promotes the formation of more densely crosslinked networks, as indicated by the higher storage modulus in Figure S1. In these densely crosslinked networks, the molecular structure is relatively irregular, containing a significant number of unreacted monomers trapped within the networks and unable to participate in further crosslinking. In BisEMA/UI copolymers, the presence of reactive diluents and relatively flexible urethane monomers influence crosslinking dynamics and facilitate double bond conversion. This explains the higher double bond conversion observed in BisEMA/UI compositions (Figure S4).

Photo-differential scanning calorimetry (Photo-DSC) was used as a complementary method to photorheology (Table S1). The results support the trends observed via photorheology. With a larger fraction of BisEMA in the formulation, rapid initial network formation is observed from a shorter time to reach the peak maximum and a higher peak value. Along with a longer time to reach 95% conversion (t_{95}) due to the immobilization of reactive groups, this confirms a rapid and inhomogeneous network formation for higher ratios of BisEMA. Calculated double bond conversions are less conclusive for this method, likely due to the oligomeric nature of UI and the associated inaccuracies in calculations based on the manufacturer-given average molecular weight. Nevertheless, a significant difference in reactive group conversion is seen between formulations with lower UI content (76%–78% conversion for 0%–20% UI) and the formulation with higher UI content (82% conversion for 50% UI).

Overall, PhIPS in these systems is governed more by the differences in the chemistries of the components than by kinetics. To demonstrate this, a custom setup was constructed to assess the onset of PhIPS and the ultimate transparency. The results (Figure 4, right) indicated that PhIPS develops rapidly after exposure to the photosensitive formulation, within 1–2 s, with shorter onset times for formulations with higher UI fractions. Moreover, the tendency to form more distinct phases and interphases, which contain balanced levels of all components, increases, as evidenced by a significant drop in transparency [52].

The observed trend toward PhIPS in BisEMA/UI formulations demonstrates that the collective differences in reactivity, polarity, and molecular weight of the involved componets, commonly referred to as solubility parameters, are substantial enough to drive PhIPS [53].

3.3 | Dynamic Mechanical Analysis

Photoinitiated crosslinking of (meth)acrylates results in complex molecular networks [54]. The irregularity of the resulting networks can be further characterized by examining the viscoelastic behavior of the polymer, which is obtainable from the DMA test [53]. In addition to the storage modulus, which reflects the material's stiffness at different temperatures, the tan δ parameter, defined as the ratio of loss to storage modulus, provides valuable information about the molecular network's architecture, damping behavior, and glass transition. For a polymer with a more uniform structure, the tan δ peak is narrow and well-defined, with a maximum associated with the glass transition temperature (T_g) [55]. Irregular networks, however, often show broad tan δ peaks [56]. The FWHM of such peaks is therefore agreed upon as a measure of the glass transition. Broadened FWHMs indicate wide crosslinking densities or the presence of different polymer phases in multicomponent systems [57]. Also, varying monomer ratios in multicomponent systems cause a shift of the tan δ toward each polymer's characteristic value, which can be considered to address the overall crosslinking qualities.

Figure 5 illustrates the tan δ curves for pure BisEMA, pure UI, as well as their mixed compositions. Pure BisEMA shows a broad glass transition range, with a maximum of around 120°C, enabling this polymer to avoid thermal softening over a wide temperature range. The storage modulus of IBOA remains high and stable (more than 3 GPa at 25°C), while the tan δ—which

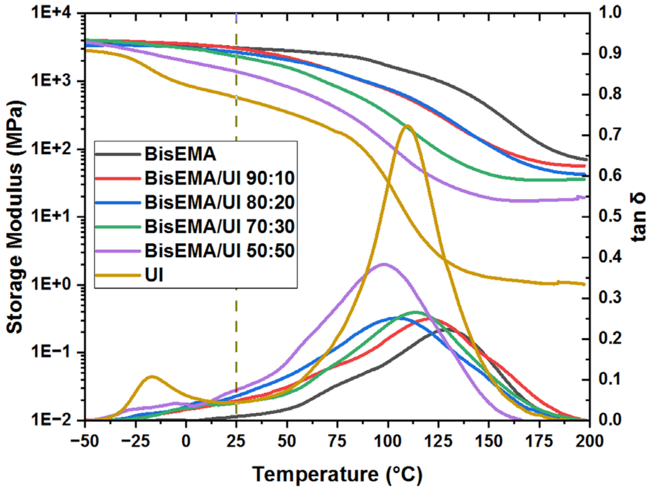

FIGURE 5 | Storage modulus and tan δ of BisEMA/UI photopolymers with different composition ratios. [Color figure can be viewed at wileyonlinelibrary.com]

represents damping properties—remains low. Therefore, not only at low temperatures but also at elevated temperatures does the polymer deliver a brittle character. The UI, on the other hand, shows distinct behavior for its components. UDA shows a rubbery character, characterized by a small tan δ peaking at −18°C. IBOA can also be characterized by a relatively sharp peak at 110°C, which is typical for many thermoplastics, knowing that it does not contribute to crosslinking reactions. The relatively high tan δ of IBOA as a brittle polymer, as well as the low one of UDA, are related to their mutual interactions in UI. The rubbery behavior of UDA at 110°C caused the polymer to show high damping at high temperatures. Likewise, the low dampening of UI at −18°C is due to IBOA, being in its glassy state at that temperature.

As the UI content increases, the fraction of IBOA in the system increases, which shows good compatibility with BisEMA as indicated by a Hansen solubility distance of 2.8. IBOA can therefore reduce the crosslink density of BisEMA and contribute to network expansion. This reduction is evident in the tan δ curve, where the peak corresponding to BisEMA shifts to lower temperatures. Despite this, the broad glass transitions observed in these systems, particularly in copolymers containing 10–30 wt.% UI, ensure maintaining good resistance to thermal softening, as demonstrated by the storage modulus values (e.g., at 25°C). Nonetheless, the high compatibility between IBOA and BisEMA significantly reduces the mobility of UDA and drives the system to undergo dual-like kinetics, including the rapid polymerization of BisEMA followed by the slower, diffusion-limited polymerization of UDA. This is further supported by photo-DSC results (Table S1), where formulations with higher BisEMA content show shorter times to reach the peak maximum and higher peak intensities, indicating rapid network formation. These are accompanied by longer times to reach 95% conversion (t_{95}), which reflects the diffusion-limited continuation of the reaction, likely involving UDA. The fast reaction of diluted BisEMA largely restricts UDA diffusion and imposes localized polymerization. This sequential polymerization behavior is further supported by the broadened tan δ transitions observed in the DMA results of

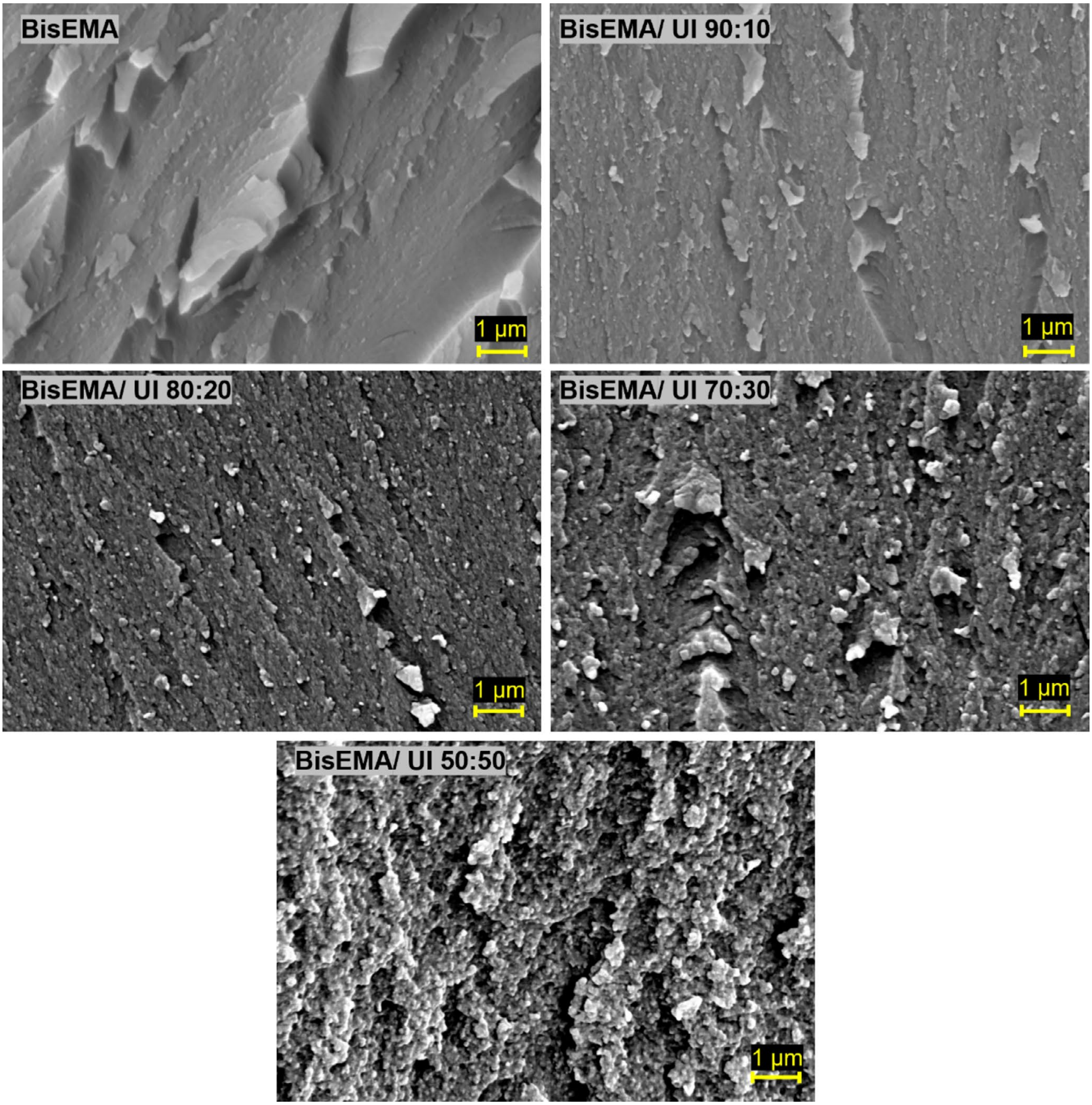

FIGURE 6 | Fracture surface of BisEMA/UI photopolymers after tensile testing. [Color figure can be viewed at wileyonlinelibrary.com]

compositions with higher UDA content (Figure 5). The morphologies of the resulting polymers will be discussed in the following section.

3.4 | Scanning Electron Microscopy

The SEM images illustrate the transition from brittle to ductile fracture across the polymer samples. As observed in Figure 6, BisEMA showed a brittle fracture surface characterized by brittle features such as cleavage planes and minimal plastic deformation. Localized crazing is the primary mechanism for energy dissipation, with no detected heterogeneity in the microstructure.

The fracture surface remains smooth in the BisEMA/UI 90:10 sample, showing minimal stretching. Moreover, the introduction of UI results in the blunt edges of the crazes (BisEMA/UI 80:20 and BisEMA/UI 70:30), indicating slight plastic deformation. The images also reveals heterogeneities, which are unaffected regions by the applied stress at the fracture plane, in the range of hundreds of nanometers.

The BisEMA/UI 80:20 sample shows a fracture that, while still brittle-like, begins to exhibit slight ductile characteristics. Pronounced microstructural heterogeneities are evident, yet the overall matrix coherence remains unchanged. Notably, the heterogeneities were not significantly larger for formulations with higher UI fractions. In contrast, the BisEMA/UI 70:30 sample

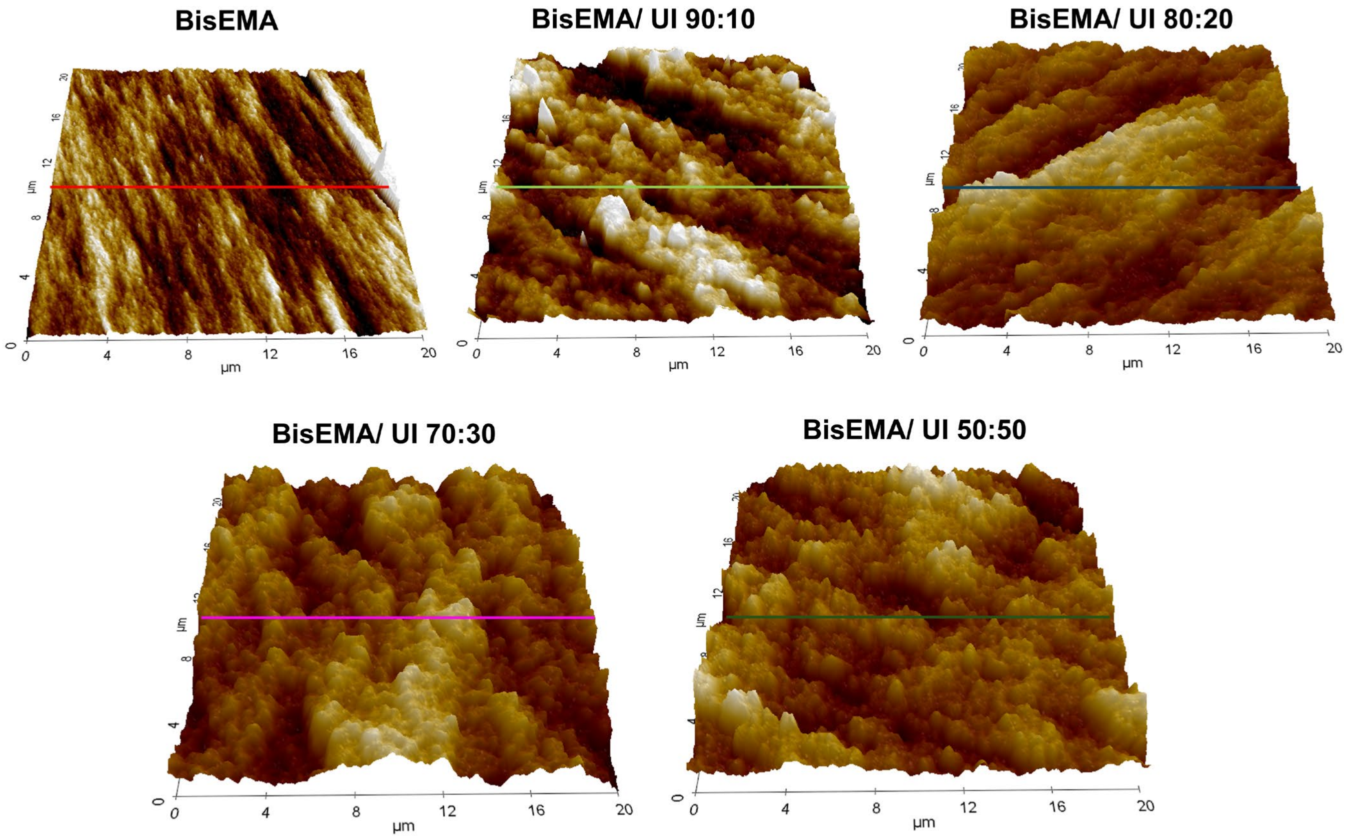

FIGURE 7 | AFM topography image of a 20×20-μm^2 region on the fracture surface of BisEMA/UI copolymers. [Color figure can be viewed at wileyonlinelibrary.com]

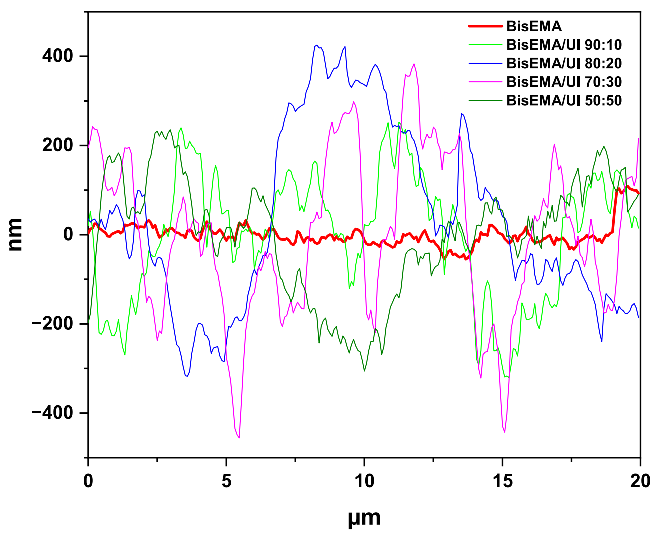

FIGURE 8 | The fracture profile along arbitrary lines of BisEMA and BisEMA/UI copolymers. The exact values of average roughness and peak to valley over the entire scanned regions are presented in Table 3. [Color figure can be viewed at wileyonlinelibrary.com]

shows a more noticeable formation of domains, visibly impacting the polymer's appearance. This sample reveals deeper cavities and curved regions, suggesting a shear-yielding mechanism rather than localized crazing [58].

The separated phase structure of sample BisEMA/UI 50:50 is characterized by a very rough microstructure, where considerable heterogeneities appear within the matrix, making their identification challenging. The presence of large interfaces between phases as well as extensive plastic deformation contributes to the dissipation of applied stress. In such a phase-separated structure, there is noticeable morphological contrast and debonding at the interfaces, which distinguish the soft phase from the rigid matrix.

TABLE 3 | 2D surface parameters: average roughness (R_a), peak-to-valley roughness (R_{pv}), and phase contrast (PC) of 20 μm^2 of BisEMA/UI copolymers at different composition ratios.

BisEMA/UI ratio	R_a (nm)	R_{pv} (nm)	PC (°)
100:00	15	213	38
90:10	127	617	76
80:20	137	939	70
70:30	188	865	116
50:50	131	720	170

3.5 | Atomic Force Microscopy

3.5.1 | Fracture Surface Analysis-Topography

Further analysis was conducted using the results from topographic results from AFM, performed in tapping mode over a 20 μm^2 area of the fractured surfaces. The findings reveal nanoscale surface roughness for all samples (Figure 7). This level of roughness is indicative of brittle fracture behavior, particularly for the pure BisEMA photopolymer, which shows the least resistance to crack propagation, as evidenced by the fracture progress trace lines (Figure 8).

The brittle fracture in this polymer is characterized by a smooth, mirror-like surface without significant irregularities or prominent features. However, the fracture surface of the BisEMA/UI copolymers exhibits evident alterations, marked by the emergence of microductilities (Figure 7) and increased surface roughness (Table 3). From a fracture mechanics perspective, the high surface roughness expressed by the average roughness (R_a) and peak-to-valley roughness (R_{pv}) can be attributed to loosely crosslinked regions surrounding highly crosslinked domains. These regions typically contain numerous weak points that are preferred sites for crack initiation and propagation [59].

Accordingly, it can be inferred that the UI crosslinked network is looser than the BisEMA network, likely due to the greater molecular distance between the UDA oligomer's double bonds. Therefore, the fracture propagates in a manner characterized by undulating patterns. The high roughness observed in BisEMA/UI copolymers can also be attributed to the different shrinkage behaviors of the respective phases [44, 60]. Compared to the UI phase, the BisEMA phase contains a higher number of covalent bonds per volume element, leading to more pronounced shrinkage and contraction, which distinguishes it from the UI phase.

3.5.2 | Fracture Surface Analysis-Phase Imaging

Besides assessing the quality of crack propagation, scanning a wide area of the fracture surface also facilitated the identification of suitable regions for phase imaging without requiring smoothing treatments, such as sample polishing or microtomy. Phase imaging visualizes the partial interactions of the oscillating cantilever with the surface and provides insights into local stiffness or rigidity contrasts across the sample. Compared to hard regions that respond elastically to tapping forces, softer areas dampen these forces, resulting in varying phase degrees—lower phases correlating with harder areas and higher phases with softer ones [22]. Subsequently, selected 2-μm^2 areas from the scanned regions were measured (Figure 9, statistical details are provided in Table 3).

As illustrated for BisEMA/UI copolymers in Figure 9, the phase separation becomes more pronounced, and the phase contrast becomes noticeable at higher UI/BisEMA ratios. The microstructure of BisEMA consists of densely packed microgels with an average size of 67 nm and a regular arrangement. The slight variations in domain size can be attributed to the distribution of highly crosslinked centers surrounded by looser crosslinks [61]. The uniform arrangement of these microgels and their small size also contribute to the transparency of BisEMA at the macroscale (Figure 4). Besides, BisEMA's surface response to tapping forces was similar, characterized by slight variations in the cantilever's phase angle upon tapping the surface (Table 3 and the histogram in Figure 9), suggesting uniform mechanical characteristics at the microscale. The morphology of the BisEMA/UI 90:10 formulation reveals larger domains, averaging approximately 200 nm in size, which are more elongated compared to pure BisEMA. Moreover, it exhibits partial embedment of the UI phase within the BisEMA matrix, evident as dark areas with lower phase degrees. This observation is further confirmed by the broader phase contrast observed in the corresponding histogram. The phase contrast, represented by the histogram obtained from tapping mode phase imaging, reflects the extent of dampening of tapping energy in localized areas on the surface, suggesting a slight presence of the second phase in the BisEMA/UI 90:10 formulation. As mentioned previously, UI contains a high molecular weight urethane acrylate oligomer. Even in low amounts, urethanes effectively participate in the crosslinking of BisEMA and promote the formation of larger microgels by enlarging the network size [23, 62].

The morphology of the BisEMA/UI 80:20 formulation does not exhibit the consistent characteristics and microstructural integrity previously identified in the pure BisEMA and BisEMA/UI 90:10 samples. Instead, it shows a more heterogeneous microstructure, with soft UI geometries within and between the rigid BisEMA phases. Considering distinct regions separated by UI, these domains possess sizes that can significantly alter the optical appearance of the material, especially at larger thicknesses.

At higher UI compositions (BisEMA/UI 70:30 and 50:50), phase separation (PhIPS) becomes more pronounced, as indicated by the phase contrast. In the 50:50 formulation, the BisEMA phase exhibits the lowest structural integrity compared to the other samples. The emergence of hard/soft interphases also becomes evident in this sample, as illustrated in the histogram. The overall morphology becomes more heterogeneous in both soft and hard phases, consistent with previous observations from DMA results.

The observed evolution of PhIPS also provides a reasonable explanation for the observed trends in turbidity (Figure 4 left). Pure BisEMA is homogeneous and shows little phase contrast, corresponding to high transparency. Slight replacement of BisEMA with UI in BisEMA/UI 90:10 and 80:20 formulations introduces more variations in refractive index, thus leading to higher turbidities. The higher fraction of UI in the BisEMA/UI 70:30 and 50:50 formulations allows for substantial light scattering as there are multiple clearly defined phases to reach the highest turbidity. Given the interconnection of soft phases at high UI content, it can be inferred that in addition to domain size, the level of interconnectivity directly influences the degree of light scattering.

3.5.3 | Cross-Sectional AFM Imaging-Polishing

To investigate the effect of the AFM tapping mechanism on imaging the variations in mechanical properties, mirror polishing and ultrasonication were performed on the fractured surfaces. Figure 10 presents the resulting set of images. Across all BisEMA/UI compositions, the ratio of setpoint amplitude to free oscillation amplitude (A/A_0) was maintained close to unity. This strict adherence to a balanced A/A_0 ratio is crucial in effective tapping to visualize surface rigidities. Additionally, amplitudes above 30 nm and low setpoint to amplitude ratios were selected to optimize tapping conditions [63].

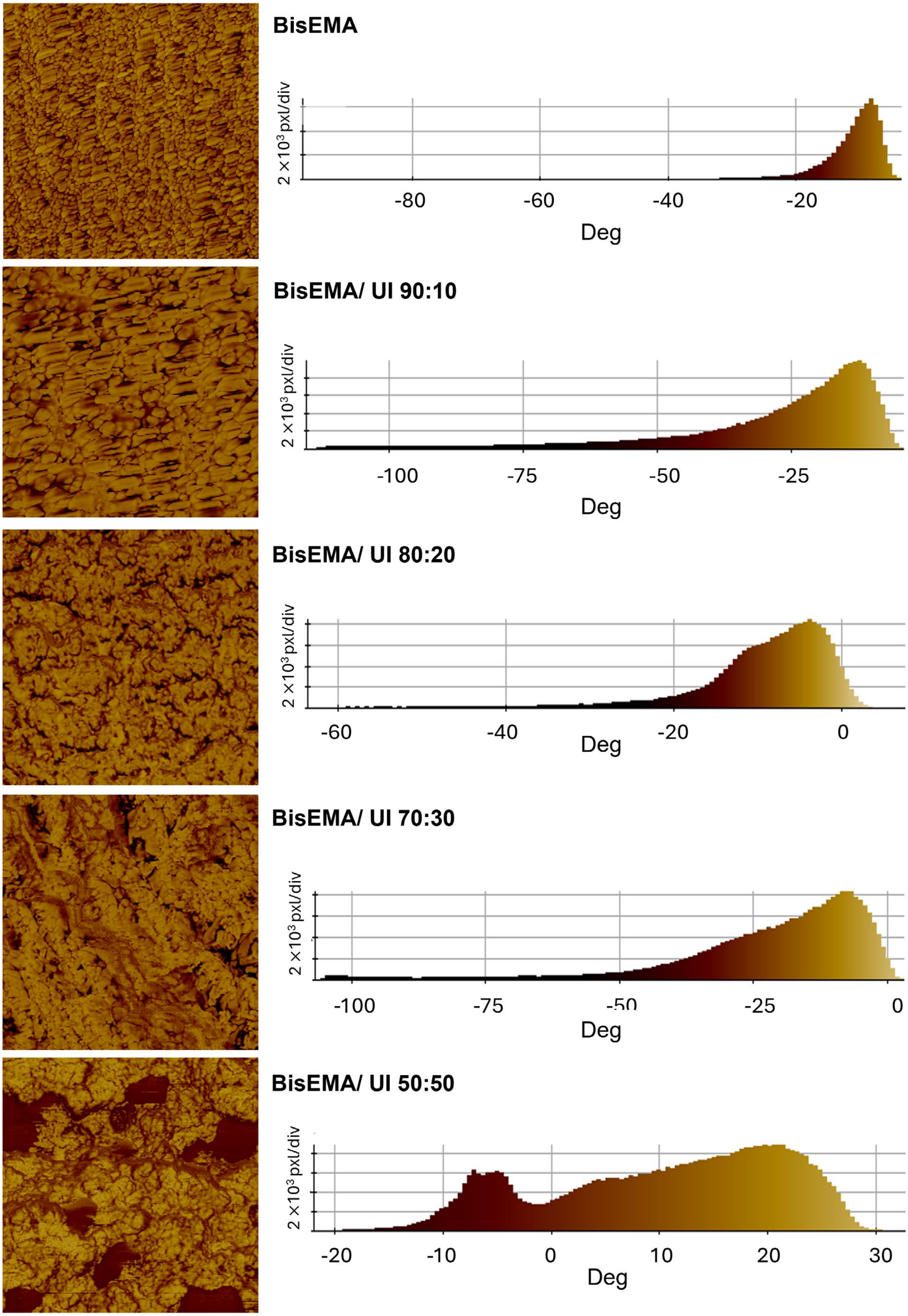

FIGURE 9 | Tapping mode AFM representation of the evolution of PhIPS within the BisEMA/UI copolymers. Each image has dimensions of 2×2 μm². [Color figure can be viewed at wileyonlinelibrary.com]

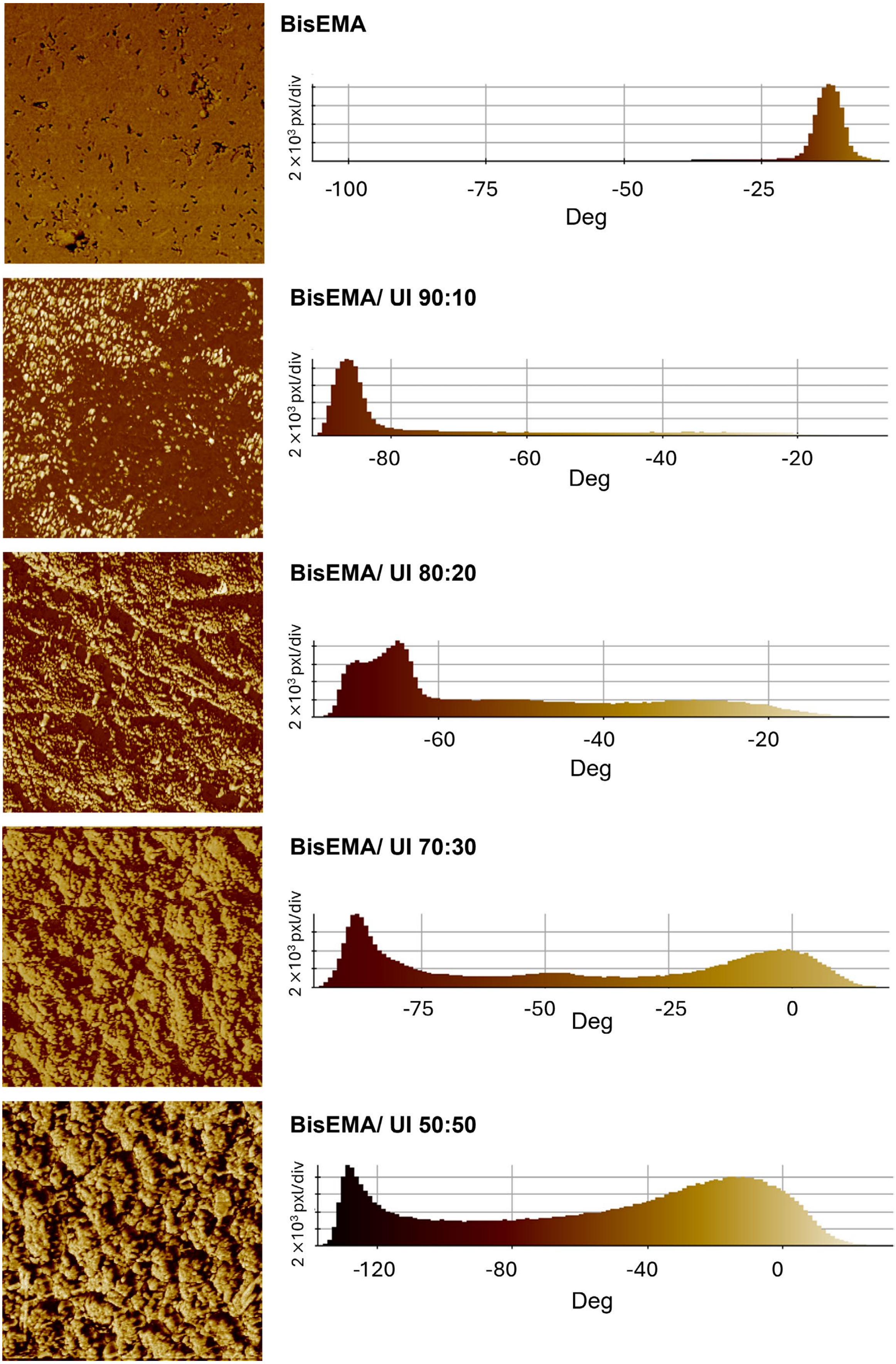

FIGURE 10 | Tapping mode phase imaging of the polished cross sections of BisEMA/UDA copolymers. Each image has dimensions of 2×2 μm^2. [Color figure can be viewed at wileyonlinelibrary.com]

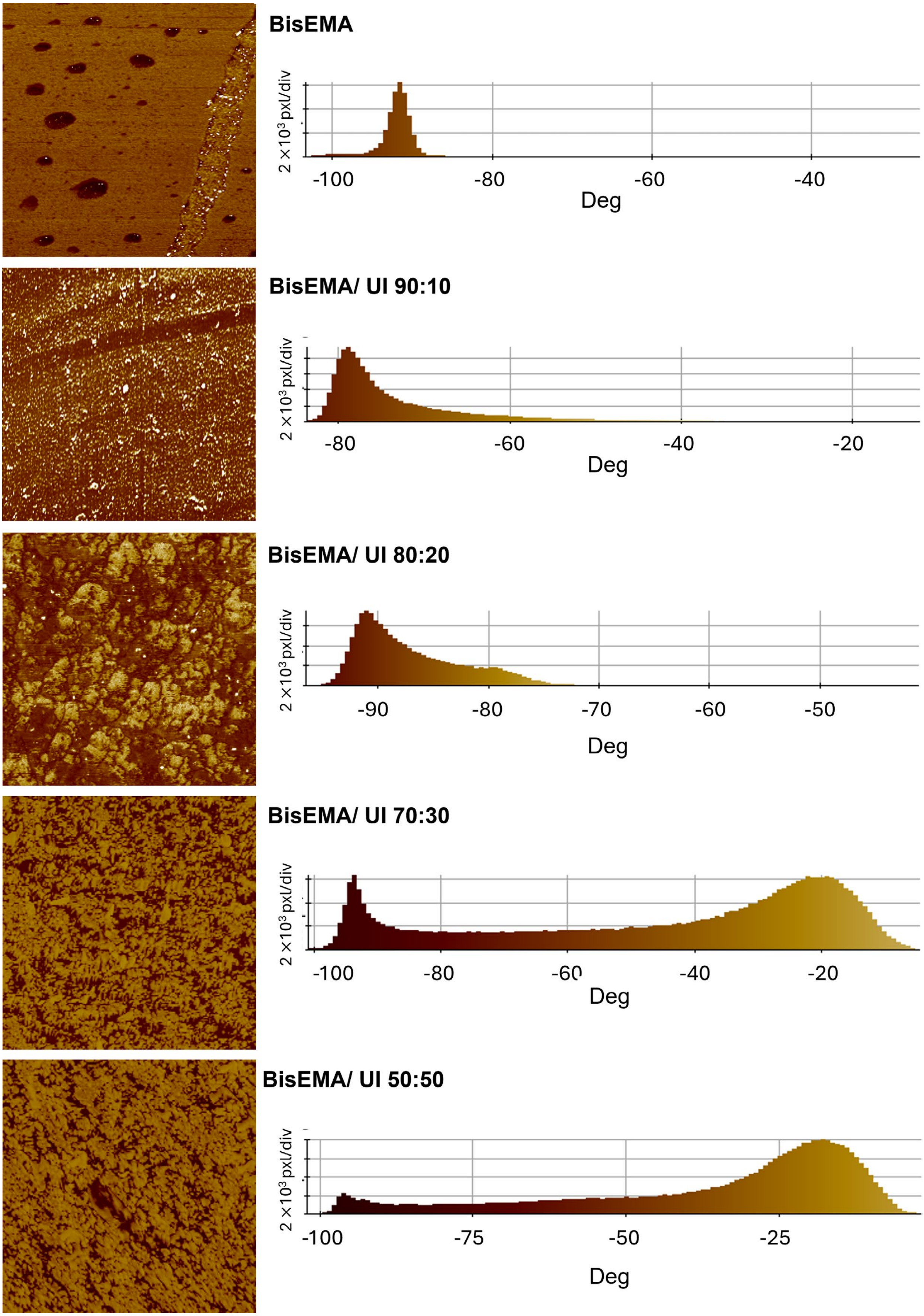

FIGURE 11 | Tapping mode phase imaging of the cross sections of BisEMA/UI phase structures obtained after (cryo)ultramicrotomy: Each image has dimensions of $2 \times 2\ \mu m^2$. [Color figure can be viewed at wileyonlinelibrary.com]

As Figure 10 shows, pure BisEMA is a monophasic structure with several microvoids averaging approximately 80 nm in size. In contrast, soft UI phases begin to appear in the BisEMA/UI 90:10 formulations, resulting in the elimination of these microvoids. This phenomenon can be attributed to the dissipation of shrinkage stresses associated with BisEMA polymerization by the presence of soft, droplet-like UI phase morphologies [44]. The development of soft phases with an increased fraction of UI in formulations (from BisEMA/UI 80:20 to 50:50) results in the formation of continuous soft phases. In the 50:50 formulation, the soft phase predominates over the BisEMA phase, and a significant interphase develops as a transition between the two phases. The development of such interphases, which contain a balanced composition of the components involved, can also be tracked by examining the generated histogram.

Although tapping mode phase imaging is inherently qualitative, the relative positioning and distribution of pixels in the phase histogram can still reflect differences in local adhesion and stiffness. For example, the phase contrast observed in pure BisEMA is relatively low (about 38°), whereas in BisEMA/UI formulations (e.g., 70:30) the contrast becomes significantly broader (Figure S5). This substantial variation suggests significant differences in mechanical properties, particularly rigidity, between the soft UI phases and the hard BisEMA phase. Notably, sorting out the concerns regarding sample preparation, such as surface smoothing, and optimizing imaging settings, particularly the A/A_0 values, provided evidence supporting the correlation of higher phase values with the soft UI, and lower phase values with the hard BisEMA phases. The histograms presented illustrate this trend clearly: from (a) to (e), increasing UI content correlates with a shift toward higher phase values in the right-side regions (yellow domains).

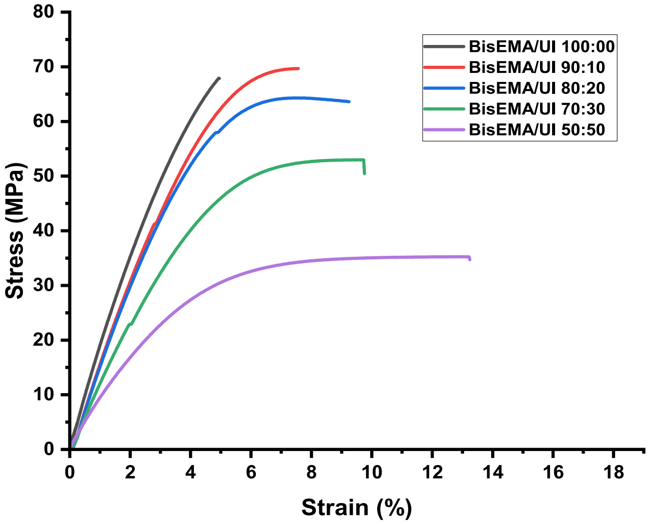

FIGURE 12 | Mechanical behavior of BisEMA/UI copolymers under tensile test. [Color figure can be viewed at wileyonlinelibrary.com]

3.5.4 | Cross-Sectional AFM Imaging-Ultramicrotomy

As mentioned above, reliable results in AFM require smooth sample surfaces, which are particularly difficult to achieve when working with heterogeneous polymers. Ultramicrotomy, employed as a technique to achieve these smooth surfaces, effectively addresses concerns about scratches and plastic deformations that can appear at small length scales after conventional polishing and grinding techniques. The AFM image series of the smooth cross sections achieved through microtomy is shown in Figure 11.

The pure BisEMA showed a uniform matrix with noticeable internal defects that facilitated brittle fracture, despite the homogeneous morphology of the matrix itself. The distribution of phase values throughout the surface indicated no significant contrast in composition density. However, distinct striations were observed, resulting from the ultramicrotome blade used in sample preparation. From the 90:10 to the 50:50 sample onward, the second phase gradually formed, as indicated by the peak on the right side of the corresponding histograms. The difference in phase degrees, which visualizes the cantilever's damping at specific areas, revealed significant differences between the soft, more adhesive phase (indicated by higher damping) and the hard matrix. Moreover, although the morphology of both phases can be slightly affected by the applied shear forces, this technique produced consistently smooth surfaces, which facilitated a more accurate correlation between the phase degrees and the material's rigidity, enhancing the reliability of the PhIPS characterization.

Like the polished samples (Figure 10), the histogram analysis of the ultramicrotome surfaces reveals that the soft UI phase shows higher degrees than the hard BisEMA matrix (Figure 11). However, these findings differ from those observed on untreated fracture surfaces. This discrepancy may be due to the qualitative nature of phase imaging and the requirement for different setpoint to amplitude (A/A_0) ratios for each measurement,

TABLE 4 | Statistical results of thermomechanical tests on BisEMA/UI photopolymers.

BisEMA/UI ratio	Strength (MPa)	Elongation at break (%)	Storage modulus at 25°C (MPa)	Impact strength (kJ mm^{-2})
100:0	67.9 ± 3.3	4.9 ± 2.5	3090	6.6 ± 0.8
90:10	69.7 ± 1.7	7.7 ± 0.9	2330	6.5 ± 1.9
80:20	63.6 ± 2.5	7.6 ± 1.2	2260	6.4 ± 1.6
70:30	53.9 ± 3.3	7.5 ± 1.9	2320	7.4 ± 2.7
50:50	36.6 ± 1.5	13.8 ± 2.6	1450	12.2 ± 0.9

which can be affected by the varying surface qualities between untreated and treated samples. The relationship between phase contrast and local rigidity is influenced by factors such as surface smoothness, the presence of residues, microvoids, and contaminants, as well as the effectiveness of the tapping force [63]. On rough or adhesive surfaces, the interaction between the oscillating tip and surface irregularities can cause misleading phase lag fluctuations that do not accurately represent surface rigidity. Therefore, quantitative AFM imaging methods are generally more reliable for precise surface properties characterization.

3.6 | Mechanical Testing

To affirm the effect of the introduced microphase separation on the mechanical performance, tensile and impact test results provide insights into the copolymers' strength and deformation behavior at low and high strain rates (Figure 12, Table 4). The pure BisEMA (BisEMA/UI 100:00) exhibited a tensile strength of approximately 70 MPa and an elongation at break of around 5%. This high strength stems from the unique chemical structure of BisEMA, which combines the rigidity of Bisphenol A with the slight flexibility provided by repetitive ethoxylated groups. The monomer's lack of voluminous side groups and relatively short aliphatic chains connecting t Bisphenol A units contribute to notable conformational flexibility and high crosslinking. The high number of covalent bonds in the system increases strength; however, increased crosslinking also reduces the network's flexibility as a trade-off. Structural defects at the molecular scale in this irregularly crosslinked polymer, along with processing-related defects such as voids, scratches, and uneven surfaces, contribute to its limited plastic deformation. Consequently, the BisEMA photopolymer exhibits relatively low elongation at break and impact resistance (Table 4).

The trends for microphase separation observed in turbidity and AFM measurements are reflected in the mechanical performance of the bulk photopolymers. Gradual replacement of BisEMA with UI in the 90:10 and 80:20 formulations improved the elongation at break without significantly affecting Young's modulus, a measure of sample stiffness, and the ultimate tensile strength remained comparable to that of pure BisEMA, with slight improvement in the 90:10 formulation.

Considering the long chain length of urethanes and their partial crosslinking with BisEMA, low-UI content (e.g., in the BisEMA/UI 90:10 and 80:20 formulations) contributes to more flexible networks with reduced crosslink densities, without compromising mechanical strength. This is reflected in the observed elongation improvements, likely due to the incorporation of flexible urethane segments into the BisEMA-rich phase, resulting in decreased network rigidity. Such mechanical behavior provides a favorable balance between flexibility and durability, which is particularly beneficial for technical polymers; nevertheless, at low-UI concentrations, impact resistance remains largely unchanged, suggesting that despite network flexibility improvements, additional energy dissipation mechanisms are required to enhance fracture toughness. AFM results confirm this by showing isolated soft domains in low-UI systems that improve the material's performance under low strain rates but are less effective in arresting crack propagation during rapid impact. A moderate increase in impact resistance is delivered by 70:30 formulation, where domain interconnection takes place, while a marked improvement is observed in the 50:50 formulation, where continuous and well interconnected soft domains become dominant and enable efficient energy dissipation, resulting in up to a 280% increase in elongation at break.

The maximum impact resistance observed in BisEMA/UI 50:50 formulation emphasizes the importance of achieving a prominent level of PhIPS and interconnections of domains for enhancing impact resistance in such copolymers.

4 | Conclusion

This study provides a comprehensive characterization of photopolymerization-induced phase separation (PhIPS) in BisEMA/UI (meth)acrylate-based photopolymer systems. Our findings demonstrate that the incorporation of UI into BisEMA leads to pronounced phase separation, which significantly affects the optical and mechanical properties of the resulting copolymers.

We monitored optical changes in photosensitive formulations during photopolymerization using a custom optical setup. Moreover, although SEM provided valuable insights into the fracture surfaces, it was less effective at distinguishing between the separated phases compared to AFM. The AFM analysis of both fracture surfaces and cross sections showed that the anticipated correlation between phase contrast and microstructure was more dependable on treated surfaces, where smoothing techniques like polishing and ultramicrotomy were employed. However, fracture surfaces did not consistently exhibit a direct correlation.

Overall, this work offers valuable insights into the development of PhIPS in (meth)acrylate photopolymers and highlights the crucial role of accurate characterization. These findings enhance our understanding of the relationship between microstructure and bulk properties in photopolymer systems, thereby advancing the development of more efficient photopolymerization processes for engineering applications.

Author Contributions

Mojtaba Ahmadi: conceptualization (equal), data curation (equal), formal analysis (lead), investigation (lead), validation (equal), visualization (lead), writing – original draft (lead). **Katharina Ehrmann:** resources (supporting), validation (equal), writing – original draft (supporting), writing – review and editing (equal). **Michael Göschl:** data curation (equal), formal analysis (equal), methodology (equal), validation (supporting). **Philipp Schlossgangl:** methodology (supporting), software (supporting), writing – review and editing (supporting). **Thomas Koch:** conceptualization (supporting), formal analysis (supporting), methodology (equal), validation (equal). **Robert Liska:** methodology (lead), resources (lead), supervision (equal), validation (equal), visualization (supporting). **Jürgen Stampfl:** conceptualization (equal), project administration (lead), resources (lead), software (lead), supervision (lead), validation (equal).

Acknowledgments

The authors gratefully acknowledge the support of the Digiphot Doctoral School for providing essential tools and resources for this project. Appreciation is also extended to Dipl.-Ings. Lisa Meissl and Florian

Mayer, who contributed to the practical aspects of the work, which significantly advanced the project's development. The authors also appreciate the support of the TU Wien Bibliothek, which covered the open access publication costs through its funding program. Open access funding provided by Technische Universitat Wien/KEMÖ.

Conflicts of Interest

The authors declare no conflicts of interest.

Data Availability Statement

The data that support the findings of this study are available from the corresponding author upon reasonable request.

References

1. A. Al Rashid, W. Ahmed, M. Y. Khalid, and M. Koç, "Vat Photopolymerization of Polymers and Polymer Composites: Processes and Applications," *Additive Manufacturing* 47 (2021): 102279.

2. A. Bagheri and J. Jin, "Photopolymerization in 3D Printing," *ACS Applied Polymer Materials* 1, no. 4 (2019): 593–611.

3. L. J. Tan, W. Zhu, and K. Zhou, "Recent Progress on Polymer Materials for Additive Manufacturing," *Advanced Functional Materials* 30, no. 43 (2020): 2003062.

4. R. Liska, M. Schuster, R. Inführ, et al., "Photopolymers for Rapid Prototyping," *Journal of Coatings Technology and Research* 4 (2007): 505–510.

5. I. M. Barszczewska-Rybarek, "A Guide Through the Dental Dimethacrylate Polymer Network Structural Characterization and Interpretation of Physico-Mechanical Properties," *Materials* 12, no. 24 (2019): 1–30.

6. S. C. Ligon, R. Liska, J. Stampfl, M. Gurr, and R. Mulhaupt, "Polymers for 3D Printing and Customized Additive Manufacturing," *Chemical Reviews* 117, no. 15 (2017): 10212–10290.

7. J. Stampfl, S. Baudis, C. Heller, et al., "Photopolymers With Tunable Mechanical Properties Processed by Laser-Based High-Resolution Stereolithography," *Journal of Micromechanics and Microengineering* 18, no. 12 (2008): 125014.

8. Q. Tran-Cong-Miyata and H. Nakanishi, "Phase Separation of Polymer Mixtures Driven by Photochemical Reactions: Current Status and Perspectives," *Polymer International* 66, no. 2 (2017): 213–222.

9. C. R. Szczepanski, C. S. Pfeifer, and J. W. Stansbury, "A New Approach to Network Heterogeneity: Polymerization Induced Phase Separation in Photo-Initiated, Free-Radical Methacrylic Systems," *Polymer* 53, no. 21 (2012): 4694–4701.

10. Y. Yamashita, K. Komori, T. Murata, et al., "Conducting Polymer Networks Synthesized by Photopolymerization-Induced Phase Separation," *Advances in Natural Sciences: Nanoscience and Nanotechnology* 9, no. 1 (2018): 015009.

11. Y. Tang, K. Wu, S. Yu, et al., "Bioinspired High-Scattering Polymer Films Fabricated by Polymerization-Induced Phase Separation," *Optics Letters* 45, no. 10 (2020): 2918–2921.

12. C. S. Pfeifer, Z. R. Shelton, C. R. Szczpanski, M. D. Barros, N. D. Wilson, and J. W. Stansbury, "Tailoring Heterogeneous Polymer Networks Through Polymerization-Induced Phase Separation: Influence of Composition and Processing Conditions on Reaction Kinetics and Optical Properties," *Journal of Polymer Science Part A: Polymer Chemistry* 52, no. 13 (2014): 1796–1806.

13. L. Zakrzewski, C. Y. Ryu, C. Bae, and C. R. Picu, "Photopolymerization-Induced Phase Separation Kinetics Explored by Intermittent Irradiation," *Polymer* 290 (2024): 126526.

14. A. Fantoni, J. Ecker, M. Ahmadi, et al., "Green Monomers for 3D Printing: Epoxy-Methacrylate Interpenetrating Polymer Networks as a Versatile Alternative for Toughness Enhancement in Additive Manufacturing," *ACS Sustainable Chemistry & Engineering* 11, no. 32 (2023): 12004–12013.

15. T. J. White, L. V. Natarajan, T. J. Bunning, and C. Allan Guymon, "Contribution of Monomer Functionality and Additives to Polymerization Kinetics and Liquid Crystal Phase Separation in Acrylate-Based Polymer-Dispersed Liquid Crystals (PDLCs)," *Liquid Crystals* 34, no. 12 (2007): 1377–1385.

16. S. Park, H.-K. Kim, and J. W. Hong, "Investigation of the Photopolymerization-Induced Phase Separation Process in Polymer Dispersed Liquid Crystal," *Polymer Testing* 29, no. 7 (2010): 886–893.

17. K. Wu, J. Yu, Y. Tang, Z. Li, G. Liang, and S. Yu, "Highly reflective porous films via polymerization-induced phase separation and application on phosphor-converted light-emitting diodes," *2020 21st International Conference on Electronic Packaging Technology (ICEPT), IEEE* (2020): 1–4.

18. D. G. Moore, L. Barbera, K. Masania, and A. R. Studart, "Three-Dimensional Printing of Multicomponent Glasses Using Phase-Separating Resins," *Nature Materials* 19, no. 2 (2020): 212–217.

19. B. Yu, Z. Huang, D. Fang, et al., "Biomimetic Porous Fluoropolymer Films With Brilliant Whiteness by Using Polymerization-Induced Phase Separation," *Advanced Materials Interfaces* 9, no. 1 (2022): 2101485.

20. B. Peng, Y. Yang, K. Gu, E. J. Amis, and K. A. Cavicchi, "Digital Light Processing 3D Printing of Triple Shape Memory Polymer for Sequential Shape Shifting," *ACS Materials Letters* 1, no. 4 (2019): 410–417.

21. V. A. Bobrin, Y. Yao, X. Shi, et al., "Nano-To Macro-Scale Control of 3D Printed Materials via Polymerization Induced Microphase Separation," *Nature Communications* 13, no. 1 (2022): 3577.

22. E. Hasa, J. P. Scholte, J. L. P. Jessop, J. W. Stansbury, and C. A. Guymon, "Kinetically Controlled Photoinduced Phase Separation for Hybrid Radical/Cationic Systems," *Macromolecules* 52, no. 8 (2019): 2975–2986.

23. S. C. Ligon-Auer, M. Schwentenwein, C. Gorsche, J. Stampfl, and R. Liska, "Toughening of Photo-Curable Polymer Networks: A Review," *Polymer Chemistry* 7, no. 2 (2016): 257–286.

24. P. Fratzl, O. Kolednik, F. D. Fischer, and M. N. Dean, "The Mechanics of Tessellations–Bioinspired Strategies for Fracture Resistance," *Chemical Society Reviews* 45, no. 2 (2016): 252–267.

25. M. Ahmadi, K. Ehrmann, T. Koch, R. Liska, and J. Stampfl, "From Unregulated Networks to Designed Microstructures: Introducing Heterogeneity at Different Length Scales in Photopolymers for Additive Manufacturing," *Chemical Reviews* 124, no. 7 (2024): 3978–4020.

26. A. Bhatia and A. K. Sehgal, "Additive Manufacturing Materials, Methods and Applications: A Review," *Materials Today Proceedings* 81 (2023): 1060–1067.

27. E. Hasa, T. Y. Lee, and C. A. Guymon, "Controlling Phase Separated Domains in UV-Curable Formulations With OH-Functionalized Prepolymers," *Polymer Chemistry* 13, no. 21 (2022): 3102–3115.

28. S. Pathreeker, F.-H. Chen, S. Biria, and I. D. Hosein, "Observation of Intensity Dependent Phase-Separation in Photoreactive Monomer–Nanoparticle Formulations Under Non-Uniform Visible Light Irradiation," *Soft Matter* 16, no. 31 (2020): 7256–7269.

29. I. Calvez, C. R. Szczepanski, and V. Landry, "Hybrid Free-Radical/Cationic Phase-Separated UV-Curable System: Impact of Photoinitiator Content and Monomer Fraction on Surface Morphologies and Gloss Appearance," *Macromolecules* 55, no. 8 (2022): 3129–3139.

30. A. Hirose, K. Shimada, C. Hayashi, H. Nakanishi, T. Norisuye, and Q. Tran-Cong-Miyata, "Polymer Networks With Bicontinuous Gradient Morphologies Resulting From the Competition Between Phase Separation and Photopolymerization," *Soft Matter* 12, no. 6 (2016): 1820–1829.

31. C. R. Szczepanski and J. W. Stansbury, "Accessing Photo-Based Morphological Control in Phase-Separated, Cross-Linked Networks

Through Delayed Gelation," *European Polymer Journal* 67 (2015): 314–325.

32. C. S. Pfeifer, N. D. Wilson, Z. R. Shelton, and J. W. Stansbury, "Delayed Gelation Through Chain-Transfer Reactions: Mechanism for Stress Reduction in Methacrylate Networks," *Polymer* 52, no. 15 (2011): 3295–3303.

33. E. Asmussen and A. Peutzfeldt, "Influence of UEDMA, BisGMA and TEGDMA on Selected Mechanical Properties of Experimental Resin Composites," *Dental Materials* 14, no. 1 (1998): 51–56.

34. I. M. Barszczewska-Rybarek, "Structure–Property Relationships in Dimethacrylate Networks Based on Bis-GMA, UDMA and TEGDMA," *Dental Materials* 25, no. 9 (2009): 1082–1089.

35. A. Szczesio-Wlodarczyk, A. Polikowski, M. Krasowski, M. Fronczek, J. Sokolowski, and K. Bociong, "The Influence of Low-Molecular-Weight Monomers (TEGDMA, HDDMA, HEMA) on the Properties of Selected Matrices and Composites Based on Bis-GMA and UDMA," *Materials* 15, no. 7 (2022): 2649.

36. J. Steindl, K. Ehrmann, C. Gorsche, et al., "Maleimide-Styrene-Butadiene Terpolymers: Acrylonitrile-Butadiene-Styrene Inspired Photopolymers for Additive Manufacturing," *Polymer International* 71, no. 7 (2022): 856–866.

37. C. Gorsche, R. Harikrishna, S. Baudis, et al., "Real Time-NIR/MIR-Photorheology: A Versatile Tool for the In Situ Characterization of Photopolymerization Reactions," *Analytical Chemistry* 89, no. 9 (2017): 4958–4968.

38. J. Bachmann, S. Schmölzer, M. A. Ruderer, G. Fruhmann, and O. Hinrichsen, "Photo-Differential Scanning Calorimetry Parameter Study of Photopolymers Used in Digital Light Synthesis," *SPE Polymers* 3, no. 1 (2022): 41–53.

39. M. Kury, K. Ehrmann, G. A. Harakály, C. Gorsche, and R. Liska, "Low Volatile Monofunctional Reactive Diluents for Radiation Curable Formulations," *Journal of Polymer Science* 59, no. 19 (2021): 2154–2169.

40. K. Sakamoto, R. Y. Lochhead, H. I. Maibach, and Y. Yamashita, *Cosmetic Science and Technology: Theoretical Principles and Applications* (Elsevier, 2017).

41. C. N. Bowman and C. J. Kloxin, "Toward an Enhanced Understanding and Implementation of Photopolymerization Reactions," *AICHE Journal* 54, no. 11 (2008): 2775–2795.

42. Y. Gu, J. Zhao, and J. A. Johnson, "A (Macro) Molecular-Level Understanding of Polymer Network Topology," *Trends in Chemistry* 1, no. 3 (2019): 318–334.

43. T. Ozaki, T. Koto, T. V. Nguyen, H. Nakanishi, T. Norisuye, and Q. Tran-Cong-Miyata, "The Roles of the Trommsdorff–Norrish Effect in Phase Separation of Binary Polymer Mixtures Induced by Photopolymerization," *Polymer* 55, no. 7 (2014): 1809–1816.

44. C. R. Szczepanski and J. W. Stansbury, "Stress Reduction in Phase-Separated, Cross-Linked Networks: Influence of Phase Structure and Kinetics of Reaction," *Journal of Applied Polymer Science* 131, no. 19 (2014); 40879.

45. G. Deng and K. A. Cavicchi, "Tuning the Viscoelastic Properties of Poly (n-Butyl Acrylate) Ionomer Networks Through the Use of Ion-Pair Comonomers," *Macromolecules* 50, no. 23 (2017): 9473–9481.

46. Y. Suzuki, D. S. Cousins, Y. Shinagawa, R. T. Bell, A. Matsumoto, and A. P. Stebner, "Phase Separation During Bulk Polymerization of Methyl Methacrylate," *Polymer Journal* 51, no. 4 (2018): 423–431.

47. C. R. Szczepanski and J. W. Stansbury, "Modification of Linear Prepolymers to Tailor Heterogeneous Network Formation Through Photo-Initiated Polymerization-Induced Phase Separation," *Polymer* 70 (2015): 8–18.

48. F. Zareanshahraki, A. Jannesari, and S. Rastegar, "Morphology, Optical Properties, and Curing Behavior of UV-Curable Acrylate-Siloxane Polymer Blends," *Polymer Testing* 85 (2020): 106412.

49. E. Hasa, J. W. Stansbury, and C. A. Guymon, "Manipulation of Crosslinking in Photo-Induced Phase Separated Polymers to Control Morphology and Thermo-Mechanical Properties," *Polymer* 202 (2020): 122699.

50. C. S. Pfeifer, "Nanostructured Multiphase Polymer Networks," in *Handbook of Nanomaterials Properties* (Springer, 2006), 1443–1460.

51. G. Odian, *Principles of Polymerization* (John Wiley & Sons, 2004).

52. W. Li, H. Cao, M. Kashima, et al., "Control of the Microstructure of Polymer Network and Effects of the Microstructures on Light Scattering Properties of UV-Cured Polymer-Dispersed Liquid Crystal Films," *Journal of Polymer Science Part B: Polymer Physics* 46, no. 19 (2008): 2090–2099.

53. C. Rocco, F. Karasu, C. Croutxé-Barghorn, et al., "Highly-Interpenetrated and Phase-Separated UV-Cured Interpenetrating Methacrylate–Epoxide Polymer Networks: Influence of the Composition on Properties and Microstructure," *Materials Today Communications* 6 (2016): 17–27.

54. Q. Tran-Cong-Miyata, T. Kinohira, D.-T. Van-Pham, A. Hirose, T. Norisuye, and H. Nakanishi, "Phase Separation of Polymer Mixtures Driven by Photochemical Reactions: Complexity and Fascination," *Current Opinion in Solid State and Materials Science* 15, no. 6 (2011): 254–261.

55. A. R. Kannurpatti, J. W. Anseth, and C. N. Bowman, "A Study of the Evolution of Mechanical Properties and Structural Heterogeneity of Polymer Networks Formed by Photopolymerizations of Multifunctional (Meth)acrylates," *Polymer* 39, no. 12 (1998): 2507–2513.

56. J. Park, J. Eslick, Q. Ye, A. Misra, and P. Spencer, "The Influence of Chemical Structure on the Properties in Methacrylate-Based Dentin Adhesives," *Dental Materials* 27, no. 11 (2011): 1086–1093.

57. A. F. Senyurt, H. Wei, C. E. Hoyle, S. G. Piland, and T. E. Gould, "Ternary Thiol– Ene/Acrylate Photopolymers: Effect of Acrylate Structure on Mechanical Properties," *Macromolecules* 40, no. 14 (2007): 4901–4909.

58. A. J. Kinloch, *Fracture Behaviour of Polymers* (Springer Science & Business Media, 2013).

59. L. Rey, J. Duchet, J. Galy, H. Sautereau, D. Vouagner, and L. Carrion, "Structural Heterogeneities and Mechanical Properties of Vinyl/Dimethacrylate Networks Synthesized by Thermal Free Radical Polymerisation," *Polymer* 43, no. 16 (2002): 4375–4384.

60. C. R. Szczepanski, T. Darmanin, and F. Guittard, "Spontaneous, Phase-Separation Induced Surface Roughness: A New Method to Design Parahydrophobic Polymer Coatings With Rose Petal-Like Morphology," *ACS Applied Materials & Interfaces* 8, no. 5 (2016): 3063–3071.

61. M. Krzeminski, M. Molinari, M. Troyon, and X. Coqueret, "Characterization by Atomic Force Microscopy of the Nanoheterogeneities Produced by the Radiation-Induced Cross-Linking Polymerization of Aromatic Diacrylates," *Macromolecules* 43, no. 19 (2010): 8121–8127.

62. I. Barszczewska-Rybarek, "The Role of Molecular Structure on Impact Resistance and Bending Strength of Photocured Urethane-Dimethacrylate Polymer Networks," *Polymer Bulletin* 74 (2017): 4023–4040.

63. G. Bar, Y. Thomann, R. Brandsch, H.-J. Cantow, and M.-H. Whangbo, "Factors Affecting the Height and Phase Images in Tapping Mode Atomic Force Microscopy. Study of Phase-Separated Polymer Blends of Poly (Ethene-Co-Styrene) and Poly (2, 6-Dimethyl-1, 4-Phenylene Oxide)," *Langmuir* 13, no. 14 (1997): 3807–3812.

Supporting Information

Additional supporting information can be found online in the Supporting Information section.